Axion-mediated photon-to-photon transitions in high-finesse dielectric resonators

Evangelos Almpanis *

Physics Division, National Technical University of Athens, GR-157 80 Zografou Campus, Athens, Greece

(Received 2 June 2025; revised 18 July 2026; accepted 23 July 2026; published 3 August 2026)

Axions are hypothetical particles that could address both the strong charge-parity problem in quantum chromodynamics and the enigmatic nature of dark matter. However, if axions exist, their mass remains unknown, and they are expected to interact very weakly with the electromagnetic field, which explains why they have not been detected yet. This study proposes a way to substantially augment the axion-photon interaction by confining the photons within high-quality-factor dielectric resonators, increasing their intensity and lifetime, and thus the possibility of interacting with axions in the background. In view of this, we study resonant axion-mediated photonic transitions in millimeter-sized spherical dielectric resonators, based on fully analytical calculations to the first order in perturbation theory. Such resonators exhibit high-lifetime Mie resonances in the microwave part of the spectrum, with a separation that can be tailored with the radius of the sphere to match the expected axion frequency, allowing axion-mediated photonic transitions when particular selection rules are fulfilled. We predict experimentally accessible axion mass regimes where such triply resonant transitions can be realized with standard dielectric resonators. We propose an experiment for probing such interactions named DARK-ROSE.

DOI: 10.1103/w9bw-zlvr

I. INTRODUCTION

One of the main mysteries in our current understanding of the physical world is dark matter, which is believed to constitute a significant portion of the total mass of the universe [1–5]. Despite its abundance and crucial role in explaining the structure and formation of the universe, dark matter remains undetected due to its weakly interacting nature. A potential candidate for this is the axion [6], an elementary particle proposed independently as a solution to the strong charge-parity ($\mathcal{CP}$) problem in quantum chromodynamics (QCD) [7]. Essentially, this problem revolves around the nonviolation of $\mathcal{CP}$ symmetry by the strong nuclear force. This is quantified by a parameter named θ, which has been measured as zero ($\leqslant 10^{-10}$) in all experiments [8], suggesting a puzzling *fine-tuning* problem. In order to solve this problem, in the 1970's Roberto Peccei and Helen Quinn proposed a new field, known as the Peccei-Quinn field [9], from which the axion particle emerges [10,11]. Given that the existence of axions offers a promising solution to both the enigmatic nature of dark matter and the strong $\mathcal{CP}$ problem, the research on them is vitally important.

*Contact author: ealmpanis@gmail.com

Published by the American Physical Society under the terms of the Creative Commons Attribution 4.0 International license. Further distribution of this work must maintain attribution to the author(s) and the published article's title, journal citation, and DOI.

Motivated by the original proposal for axions discussed earlier, the concept was extended beyond the strict framework of QCD, leading to proposals that constitute a broader class of axionlike elementary particles [6,7,12–19] that serve more general theoretical and observational purposes. The common property of all axion and axionlike particles is that they are bosons that interact very weakly with the electromagnetic (EM) field through a mixing between the electric and the magnetic field. Interestingly, such a mixing of the electric and the magnetic field is possible (without the need for cosmic axions) in exotic solid-state materials, so-called magnetoelectric (ME) or Tellegen materials. This class of materials was first conceptually conceived by Tellegen [20], while independently, the ME effect (equivalent to Tellegen) was conceptualized by Landau and Lífshíts [21] and predicted in Cr_2O_3 by Dzyaloshinskii [22], followed by experimental verifications [23]. However, until now, the observed ME phenomena are negligible in most materials with the exception of certain topological insulators, also called *axion insulators* [24–27], and more specifically, the antiferromagnetically doped topological insulators, where *axion quasiparticles* can arise due to the intrinsic magnetic properties and the unique structure of the material [28–31].

Now, a possible enhanced coupling between axion quasiparticles (solid-state axions) and cosmic axions [28,29] has generated proposals for a new generation of cosmic axion detectors named TOORAD (topological resonant axion detection) [32]. We note here that searching for cosmic axions is like tuning a radio: it needs a specific frequency but we do not know what that frequency is (where the role of the frequency is played by the mass of the axion). In this respect, the TOORAD experiment will search for cosmic axions with a mass of 0.7–3.5 meV$/c^2$, it complements, rather than replaces, more established experimental avenues such as haloscopes and helioscopes. Haloscopes, like ADMX [33–35], are designed to detect axions from the Galactic dark matter halo (masses $\sim\mu$eV$/c^2$) by converting them into photons inside a microwave cavity tuned to the axion mass. More recently, dielectric Haloscopes [36,37] and plasma Haloscopes [38–40] have also been proposed. In contrast, helioscopes such as CAST [41,42] and the next-generation IAXO [43,44] aim to detect axions produced in the Sun via their conversion into x-rays in a strong magnetic field. Together, these approaches, along with others, cover complementary regions of the axion parameter space.

If axions (pseudoscalar bosons with spin $\mathcal{S} = 0$) exist, they will interact with the photon (vector boson with spin $\mathcal{S} = 1$) in a very specific way. A photon γ_i could absorb an axion α to produce a photon γ_f with increased frequency, i.e., $\gamma_\mathrm{i} + \alpha \to \gamma_\mathrm{f}$. Alternatively, a photon γ_i could produce an axion α and a photon γ_f with a lower frequency ($\gamma_\mathrm{i} \to \gamma_\mathrm{f} + \alpha$). Such processes that involve two photons and one axion [45] are obviously allowed and can be viewed as axion-mediated transitions from photon γ_i to photon γ_f. We note here that for photons with energies in the $\sim\mu$eV scale that we will consider in this work, the momentum is on the order of $\sim\mu$eV$/c$, while the momentum of nonrelativistic dark matter axions (like the ones investigated with Haloscopes [36]) with mass $\sim\mu$eV$/c^2$ is expected to be on the order of $\sim$neV$/c$, which is negligibly small compared to that of the photons. In view of this, the axion acts as an energy reservoir, enabling photonic transitions without significant momentum mismatch [46].

Since the axion-photon-photon coupling constant $g_{\alpha\gamma\gamma}$ is very small, here we propose a strategy to substantially enhance the photon intensity and lifetime inside a high quality-factor (Q) dielectric resonator, increasing in this way the probability for axion-photon interactions when axions with specific mass exist in the background, and particular selection rules are being respected. A conceptually related approach employing (super)conducting cylindrical cavities was discussed in Refs. [47–49]; however, here we extend the concept to all-dielectric spherical resonators, providing fully analytical calculations to first order in perturbation theory and deriving the corresponding selection rule based on group theory. At first, in Sec. II we define the distinct multipolar eigenstates of the electromagnetic field inside a spherical dielectric resonator. In Sec. III, we come up with the axion-photon interaction expressed through a new term in the Maxwell Lagrangian. In Sec. IV, we set up the resonant axion-mediated photonic transitions evaluated to first order in perturbation theory and establish the selection rules that govern such transitions. This approach is sufficient for our purposes, while at the same time allowing for a deeper insight into the underlying physics. In

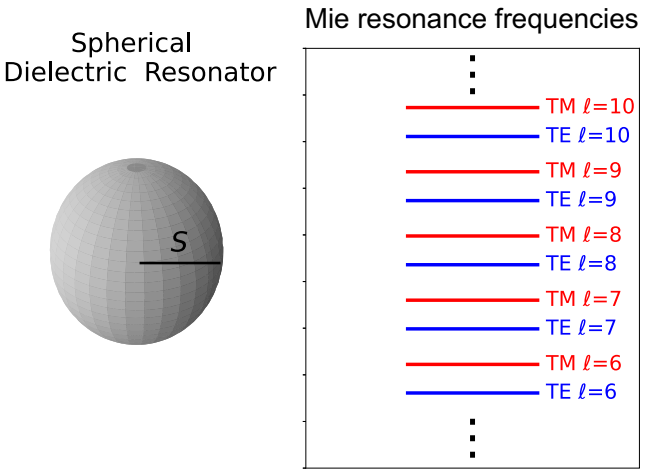


FIG. 1. Discrete photonic Mie resonance frequencies for a spherical dielectric resonator of radius S corresponding to fundamental ($\nu = 1$) TE (blue) and TM (red) modes of angular momentum ℓ. The dots indicate the presence of additional modes beyond the displayed range.

Sec. V, which is devoted to the discussion of our results, we provide our fully analytical calculations for the enhancement of the axion-mediated photonic transition rates in the presence of an optical resonator and give specific results. The last section summarizes the main findings of the paper.

II. PHOTONIC RESONANCE FREQUENCIES OF A SPHERICAL MIE RESONATOR

We will consider a homogeneous and isotropic dielectric sphere (relative permittivity ϵ, relative permeability μ) of radius S in air (free space permittivity ϵ_0, free space permeability μ_0). Scattering of light by such a sphere can be solved analytically in the framework of Mie theory [50–52], assuming a spherical expansion of both incoming and outgoing fields. By doing so, multiple peaks appear in the corresponding scattering cross-section spectrum, the so-called optical Mie resonances. Each Mie mode is characterized by the polarization type: magnetic type (transverse electric, TE) or electric type (transverse magnetic, TM), the angular momentum index ℓ, and the magnetic number m. We note here that due to spherical symmetry, these modes are degenerate ($2\ell + 1$ degeneracy). Although these modes have a finite lifetime, when the refractive index of the scatterer is high and the losses are small, the lifetime is long, leading to measured quality factors on the order of $Q \sim 10^1$–10^3 for materials such as silicon [53], titania [54,55], alumina [56,57], or other novel ceramics [58] for small multipole indices ($\ell \lesssim 5$), depending on the particle size and the frequency band. The quality factor of the resonances scales with the ℓ index [59], while for high values of ℓ [whispering gallery modes (WGMs)] the measured quality factors are on the order of $\sim 10^5$–10^{10} [60–65]. We note here that these quality factors correspond to room temperature. Throughout this work, we restrict our analysis to fundamental modes with radial index $\nu = 1$. In Fig. 1, we schematically show the resonance frequencies of the different spectrally separated Mie modes of a spherical dielectric resonator. The electric and magnetic fields, inside the sphere, of a TE mode with resonance frequency ω_1 are given by the expressions [66–68]

$$\begin{aligned}\mathbf{E}_{M\ell m}(\mathbf{r};\omega_1) &= a_{M\ell m} j_\ell(q_1 r)\mathbf{X}_{\ell m}(\hat{\mathbf{r}}),\\ \mathbf{B}_{M\ell m}(\mathbf{r};\omega_1) &= -i\frac{\sqrt{\epsilon\mu}}{q_1 c} a_{M\ell m}\nabla\times(j_\ell(q_1 r)\mathbf{X}_{\ell m}(\hat{\mathbf{r}})),\end{aligned} \tag{1}$$

TABLE I. Character table of the O(3) Lie group ($\ell = 1, 2, 3, \ldots$). R_θ are rotation operations through an angle θ ($\theta \in [0, \pi]$) about an axis, and $\mathcal{I}$ is the inversion operation.

$O(3)$	R_θ	$\mathcal{I}R_\theta$
$D_{\mathrm{g}}^{(\ell=0)}$	1	1
$D_{\mathrm{u}}^{(\ell=0)}$	1	-1
$D_{\mathrm{g}}^{(\ell)}$	$\frac{\sin(2\ell+1)\theta/2}{\sin\theta/2}$	$\frac{\sin(2\ell+1)\theta/2}{\sin\theta/2}$
$D_{\mathrm{u}}^{(\ell)}$	$\frac{\sin(2\ell+1)\theta/2}{\sin\theta/2}$	$-\frac{\sin(2\ell+1)\theta/2}{\sin\theta/2}$

while those of a TM mode with resonance frequency ω_2 are given by the expressions

$$\mathbf{E}_{E\ell m}(\mathbf{r};\omega_2) = \frac{i}{q_2} a_{E\ell m} \nabla \times (j_\ell(q_2 r)\mathbf{X}_{\ell m}(\hat{\mathbf{r}})),$$
$$\mathbf{B}_{E\ell m}(\mathbf{r};\omega_2) = \frac{\sqrt{\epsilon\mu}}{c} a_{E\ell m} j_\ell(q_2 r)\mathbf{X}_{\ell m}(\hat{\mathbf{r}}), \tag{2}$$

where $q_{1,2} = \omega_{1,2}\sqrt{\epsilon\mu}/c$, $c = 1/\sqrt{\epsilon_0\mu_0}$ being the velocity of light in vacuum; j_ℓ are the spherical Bessel functions that are finite everywhere; and $\mathbf{X}_{\ell m}(\hat{\mathbf{r}})$ are the vector spherical harmonics, $\sqrt{\ell(\ell+1)}\mathbf{X}_{\ell m}(\hat{\mathbf{r}}) \equiv -i\mathbf{r} \times \nabla Y_{\ell m}(\hat{\mathbf{r}})$. The expansion coefficients $a_{P\ell m}$, $P = E, M$, have units of electric field (V/m).

The symmetry group of a spherical particle, which involves both proper and improper rotations, is the O(3) Lie group. The character table of the O(3) group is shown in Table I. The subscripts g (gerade) and u (ungerade) denote the parity of the multipole, i.e., g for even parity and u for odd parity. We note here that if we assign the index $P = 1$ for magnetic multipoles (TE) and $P = 2$ for electric multipoles (TM), then the sum $P + \ell$ defines the parity of the Mie mode (even or odd) [68,69].

III. AXION-PHOTON INTERACTION

The interaction between axion and photon is described by an additional term in the Maxwell Lagrangian [8,45,70–74] (Lagrangian density, units $\mathrm{eV/m^3}$)

$$\mathcal{L}_{\alpha\gamma\gamma} = -g_{\alpha\gamma\gamma}\alpha(\mathbf{r},t)\mathbf{E}\cdot\mathbf{B}, \tag{3}$$

where $\alpha(\mathbf{r},t)$ is the axion field in units of eV, $g_{\alpha\gamma\gamma} = \tilde{g}_{\alpha\gamma\gamma}/\mu_0 c$, where $\tilde{g}_{\alpha\gamma\gamma}$ is the axion-photon-photon coupling constant expressed in units eV^{-1}. We note here that, although the factor $1/\mu_0 c$ is taken as unity in natural units, it must be explicitly included when working in the SI system [38,73,75,76], as we do throughout this paper. In the presence of this term, the Maxwell equations, in a linear medium (ϵ, μ) without conventional [77] free sources (the axionic terms now play the role of sources), can be recast as follows [8,72,73,78]:

$$\nabla\cdot(\epsilon_0\epsilon\mathbf{E}) = g_{\alpha\gamma\gamma}\mathbf{B}\cdot\nabla\alpha(\mathbf{r},t), \quad \nabla\cdot\mathbf{B} = 0\,,$$
$$\nabla\times\mathbf{E} = -\frac{\partial\mathbf{B}}{\partial t}, \quad \nabla\times\left(\frac{1}{\mu_0\mu}\mathbf{B}\right) = \frac{\partial(\epsilon_0\epsilon\mathbf{E})}{\partial t} + g_{\alpha\gamma\gamma}\left(\mathbf{E}\times\nabla\alpha(\mathbf{r},t) - \frac{\partial\alpha(\mathbf{r},t)}{\partial t}\right), \tag{4}$$

whereby by setting the following constitutive relations:

$$\mathbf{D} = \epsilon_0\epsilon\mathbf{E} - g_{\alpha\gamma\gamma}\alpha(\mathbf{r},t)\mathbf{B}, \tag{5}$$

$$\mathbf{H} = \frac{1}{\mu_0\mu}\mathbf{B} + g_{\alpha\gamma\gamma}\alpha(\mathbf{r},t)\mathbf{E}, \tag{6}$$

we obtain the following set of equations:

$$\nabla \cdot \mathbf{D} = 0, \quad \nabla \cdot \mathbf{B} = 0\,,$$
$$\nabla \times \mathbf{E} = -\frac{\partial \mathbf{B}}{\partial t}, \quad \nabla \times \mathbf{H} = \frac{\partial \mathbf{D}}{\partial t}. \tag{7}$$

Equation (7) is identical to the common Maxwell equations in matter [77] (without free sources). This is analogous to light traveling in an *axionic* medium [27,78] that mixes the **E** and **B** fields.

IV. AXION-MEDIATED PHOTONIC TRANSITIONS

In the case of cold dark matter, the axion can be considered as a coherent pseudoscalar classical field [28,29,32,79]

$$\alpha(\mathbf{r}, t) = A(\mathbf{r}) \cos \Omega_\alpha t, \tag{8}$$

where $\Omega_\alpha = m_\alpha c^2/\hbar$ is the axion angular frequency and m_α is the axion mass. In this treatment, we approximate the galactic axion field as monochromatic, since its expected quality factor is very large, namely, $Q_\alpha \sim 10^6$ [80–82]. Since the axionic field varies in time with angular frequency Ω_α, it can induce inelastically scattered light beams with angular frequencies $\omega - \Omega_\alpha$ (Stokes) and $\omega + \Omega_\alpha$ (anti-Stokes), as in typical Brillouin (inelastic) scattering of light by matter excitations [67,83–87]. In the special case where ω is a resonance frequency of the photonic resonator and $\omega \pm \Omega_\alpha$ is also a (discrete) resonance frequency of the resonator, the so-called (triply) resonant transitions can occur [88–92], provided that this is allowed by symmetry (as we shall see later on). We now proceed by modeling this interaction. The constitutive relations (5) and (6) can be cast as a linear system in matrix form as follows:

$$\begin{pmatrix} \mathbf{D} \\ \mathbf{H} \end{pmatrix} = \begin{pmatrix} \epsilon_0 \epsilon & -g_{\alpha\gamma\gamma}\alpha(\mathbf{r}, t) \\ g_{\alpha\gamma\gamma}\alpha(\mathbf{r}, t) & \frac{1}{\mu_0 \mu} \end{pmatrix} \begin{pmatrix} \mathbf{E} \\ \mathbf{B} \end{pmatrix}, \tag{9}$$

where the 2×2 matrix consists of one static part and one time-dependent part, as follows:

$$\begin{pmatrix} \epsilon_0 \epsilon & -g_{\alpha\gamma\gamma}\alpha(\mathbf{r}, t) \\ g_{\alpha\gamma\gamma}\alpha(\mathbf{r}, t) & 1/\mu_0 \mu \end{pmatrix} = \begin{pmatrix} \epsilon_0 \epsilon & 0 \\ 0 & 1/\mu_0 \mu \end{pmatrix} + \begin{pmatrix} 0 & -g_{\alpha\gamma\gamma}\alpha(\mathbf{r}, t) \\ g_{\alpha\gamma\gamma}\alpha(\mathbf{r}, t) & 0 \end{pmatrix}. \tag{10}$$

By assuming $\exp(-i\omega t)$ time dependence of the fields, we write the corresponding classical Hamiltonian (energy) density in the following form:

$$\begin{aligned} \mathcal{H} &= \frac{1}{4}(\mathbf{E}^* \cdot \mathbf{D} + \mathbf{B}^* \cdot \mathbf{H}) = \frac{1}{4}\begin{pmatrix} \mathbf{E}^* & \mathbf{B}^* \end{pmatrix}\begin{pmatrix} \mathbf{D} \\ \mathbf{H} \end{pmatrix} \\ &= \frac{1}{4}\begin{pmatrix} \mathbf{E}^* & \mathbf{B}^* \end{pmatrix}\begin{pmatrix} \epsilon_0 \epsilon & 0 \\ 0 & 1/\mu_0 \mu \end{pmatrix}\begin{pmatrix} \mathbf{E} \\ \mathbf{B} \end{pmatrix} + \begin{pmatrix} \mathbf{E}^* & \mathbf{B}^* \end{pmatrix}\frac{g_{\alpha\gamma\gamma}\alpha(\mathbf{r}, t)}{4}\begin{pmatrix} 0 & -1 \\ 1 & 0 \end{pmatrix}\begin{pmatrix} \mathbf{E} \\ \mathbf{B} \end{pmatrix} \\ &\equiv \mathcal{H}_0 + \delta\mathcal{H}(t), \end{aligned} \tag{11}$$

with the star denoting complex conjugation. The $\mathcal{H}_0$ is a typical Hamiltonian density for an electromagnetic wave traveling in a linear medium [77] having relative permittivity ϵ and relative permeability μ (unperturbed Hamiltonian), while the term $\delta\mathcal{H}(t)$ that contains all the *axionic* information can be considered as a small time-dependent perturbation. The axion-mediated photonic transitions arise from this dynamical perturbation of the system.

Since the axion-photon coupling is very weak, we can apply the Born approximation up to the first order to calculate the transition amplitudes. In view of this, the useful information is

provided by the overlap integral G (transition matrix element), where the perturbation matrix $\delta\hat{V}(t)$ is sandwiched between the final and initial states, i.e, $G = \langle \mathrm{f}|\, \delta\hat{V}(t)\, |\mathrm{i}\rangle$, where

$$|\mathrm{i}\rangle = \begin{pmatrix} \mathbf{E}_\mathrm{i} \\ \mathbf{B}_\mathrm{i} \end{pmatrix} e^{-i\omega_\mathrm{i} t}, \tag{12}$$

$$\langle \mathrm{f}| = (\mathbf{E}_\mathrm{f}^* \quad \mathbf{B}_\mathrm{f}^*) e^{i\omega_\mathrm{f} t}, \tag{13}$$

and

$$\delta\hat{V}(t) = g_{\alpha\gamma\gamma} \frac{A(\mathbf{r})\cos(\Omega_\alpha t)}{4} \begin{pmatrix} 0 & -1 \\ 1 & 0 \end{pmatrix} = \frac{g_{\alpha\gamma\gamma} A(\mathbf{r})}{2} \begin{pmatrix} 0 & -1 \\ 1 & 0 \end{pmatrix} (e^{-i\Omega_\alpha t} + e^{i\Omega_\alpha t}). \tag{14}$$

The overlap integral (transition matrix element) reads

$$G = \pi[\delta(\omega_\mathrm{i} - \omega_\mathrm{f} + \Omega_\alpha) + \delta(\omega_\mathrm{i} - \omega_\mathrm{f} - \Omega_\alpha)]g, \tag{15}$$

where

$$g = g_{\alpha\gamma\gamma} \int_V \mathrm{d}^3 r A(\mathbf{r})(\mathbf{B}_\mathrm{f}^*(\mathbf{r}) \cdot \mathbf{E}_\mathrm{i}(\mathbf{r}) - \mathbf{E}_\mathrm{f}^*(\mathbf{r}) \cdot \mathbf{B}_\mathrm{i}(\mathbf{r})). \tag{16}$$

The δ functions in Eq. (15) express energy conservation in the optical transitions that involve absorption and emission of one axion by a photon. The volume V is taken as the volume of the sphere since the electromagnetic field decays rapidly outside of the resonator.

Now, it is straightforward to show that $\delta\hat{V}$ remains invariant under proper rotations R_θ, while changes sign under inversions ($\mathcal{I}$) and improper rotations ($\mathcal{I}R_\theta$), since $A(\mathbf{r})$ is a pseudoscalar, i.e., $A(\mathbf{r}) \xrightarrow{E,\, R_\theta} 1 \cdot A(\mathbf{r})$ and $A(\mathbf{r}) \xrightarrow{\mathcal{I},\, \mathcal{I}R_\theta} -1 \cdot A(\mathbf{r})$. Therefore, $\delta\hat{V}$ is an irreducible tensor operator, which has the symmetry of the $D_\mathrm{u}^{(\ell=0)}$ irreducible representation of the Lie group O(3). This means that $\delta\hat{V}$ operating on an eigenvector of the $P\ell$ irreducible subspace, transforms according to the relevant direct product representation

$$D_\mathrm{u}^{(\ell=0)} \otimes D_\mathrm{g}^{(\ell)} = D_\mathrm{u}^{(\ell)}, \quad D_\mathrm{u}^{(\ell=0)} \otimes D_\mathrm{u}^{(\ell)} = D_\mathrm{g}^{(\ell)}. \tag{17}$$

These considerations lead to a straightforward selection rule for the photonic transitions described above: the photonic mode must undergo a change in parity, while the angular momentum index ℓ remains conserved, for axion absorption (anti-Stokes) and axion emission (Stokes) processes. In Fig. 2, we show a schematic representation of axion-mediated photonic transitions with respect to the mentioned selection rule, provided that the frequency difference of the optical modes is $\Delta f = \Omega_\alpha/2\pi$, where $\Omega_\alpha/2\pi$ is the frequency of the axion. In the left-hand panel, we show the anti-Stokes process, where an axion is absorbed by the photonic transition from the TE_ℓ mode with lower frequency to the TM_ℓ mode with higher frequency, while in the right-hand panel we show the inverse process (Stokes) where an axion is emitted by the photonic transition from the TM_ℓ mode with higher energy to the TE_ℓ mode with lower energy. We also note that the same selection rule is deduced by explicitly (analytically) doing the algebra for the $\int \mathbf{B}^*_{\mathrm{f};P\ell m} \cdot \mathbf{E}_{\mathrm{i};P'\ell'm'}$ and $\int \mathbf{E}^*_{\mathrm{f};P\ell m} \cdot \mathbf{B}_{\mathrm{i};P'\ell'm'}$ products and making use of the angular integration properties of the vector spherical harmonics. We note here that these integrals also produce a factor $\delta_{mm'}$, which implies that the initial and final photon modes must have the same azimuthal index m. In scatterers of perfectly spherical shape, this index is degenerate, whereas in realistic experiments this degeneracy is typically lifted by small asymmetries such as weak deformations from the spherical shape, localized coupling elements (loop or prism couplers) positioned at fixed azimuthal angles, or controlled surface defects, among others.

V. RESULTS AND DISCUSSION

We now assume a spherical lossless high-index dielectric particle of radius S in air. The relative dielectric permittivity of the sphere is $\epsilon = 12$, while its relative magnetic permeability is $\mu = 1$.

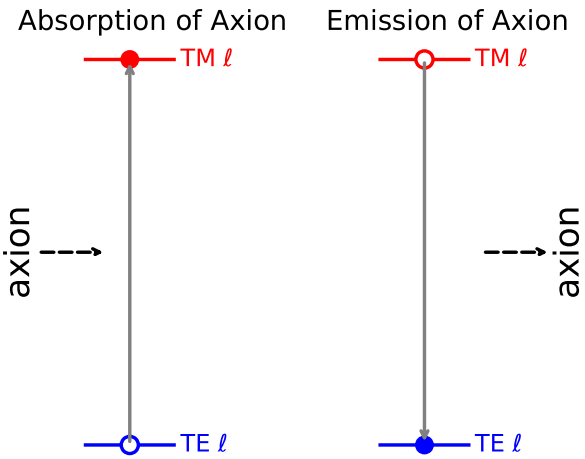


FIG. 2. Schematic representation of axion-induced photonic transitions between electromagnetic modes in a spherical resonator. Left: An axion is absorbed, enabling a transition from a TE mode to TM mode with the same angular momentum ℓ. Right: The reverse process, where a transition from TM to TE mode is accompanied by the emission of an axion. The initial and final photonic states are marked with open and solid circles, respectively, while axions are represented by dashed arrows.

We will present our results in scaled units of the radius S, nevertheless the radius S can vary from microns to centimeters, depending on the targeted frequency range (we will give specific examples later). As discussed earlier, such particles support long-lifetime, spectrally separated, Mie modes of the EM field, characterized by the indices P and ℓ. For spherical particles, the resonant frequencies can be calculated analytically using the T-matrix formulation, which is evaluated on the particle's boundaries [93]. Consequently, the refractive index of the surrounding medium shifts the resonant frequencies accordingly. Since in such particles the TE_ℓ mode has always lower energy than the corresponding TM_ℓ mode [51] (see Fig. 1), as the initial state we set the ℓ multipole of magnetic type (TE) and as the final state we take the ℓ multipole of electric type (TM), for the axion absorption process, to comply with the selection rule. The frequency difference between the initial and final states must be adjusted to the axion frequency, $f_\mathrm{f} - f_\mathrm{i} = \Omega_\alpha/2\pi$, to obtain the resonant transition. We note here that the reverse process (axion emission) is also possible, as shown in the right-hand panel of Fig. 2, and the transition matrix element is the same, so we will not discuss it for time saving.

In Fig. 3(a), we show the corresponding resonance frequencies for both the TE and TM modes, in scaled units, versus the ℓ index, for ℓ ranging from 6 to 10. Such values of ℓ are typical for high-Q Mie modes. We see an almost linear increase in the Mie mode frequencies with increasing ℓ. In Fig. 3(b), we show the scaled frequency difference $\Delta f S/c$ of modes with the same ℓ. We see that it remains almost constant $\Delta f S/c \simeq 0.05$. This means that for axion masses in the range of $\sim\mu\mathrm{eV}/c^2$, the particle radius would be in the millimeter scale, while the EM radiation will be in the microwave range. Such spherical resonators exhibiting Mie modes can be fabricated and measured experimentally using microwave radiation [55–57,94]. Microwave coupling to and from the dielectric resonator can be achieved using a small loop or dipole antenna placed in the near field, enabling efficient excitation and extraction of the desired resonant modes. The output (converted) photons may be collected by a frequency- and polarization-selective antenna optimized for the corresponding mode, as commonly realized in microwave resonator experiments. Since the frequency separation between the initial and final photons is on the order of hundreds of megahertz, well above the typical bandwidth of both the pump and the detector, no interference between the input and output signals is expected. This separation is further reinforced by the fact that the two signals also possess opposite polarization signatures. We note also here that no external

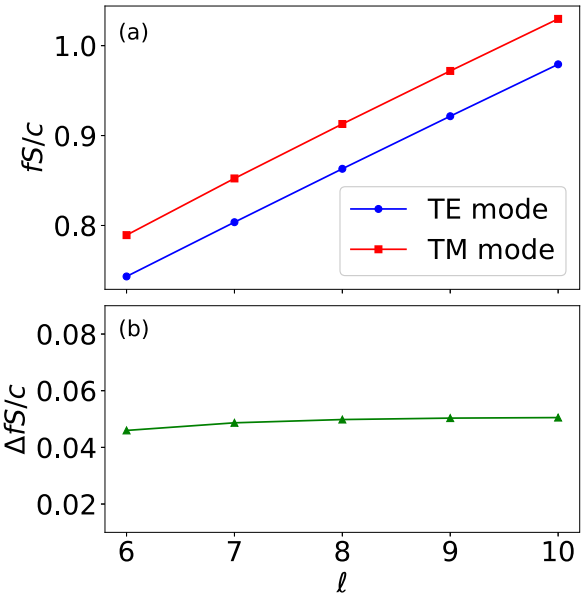


FIG. 3. (a) Scaled resonance frequencies (fS/c) for TE and TM modes of the spherical dielectric resonator under consideration as a function of the angular momentum index ℓ. The data highlight the splitting between TE_ℓ and TM_ℓ modes at each ℓ. (b) The corresponding frequency difference $\Delta fS/c = (f_{\mathrm{TM}_\ell} - f_{\mathrm{TE}_\ell})S/c$, quantifying the frequency difference as a function of ℓ.

static magnetic field has to be applied in the proposed setup. We emphasize that the proposed platform is fully scalable and can be adjusted to the targeted axion mass. In Table II, we show the correspondence guidelines toward the selection of the resonator parameters for targeted axion searches.

Furthermore, by targeting a specific mass window (e.g., an octave), it is possible to scan a portion of this window while keeping the resonator size constant and varying the refractive index of the surrounding medium instead. For example, embedding the resonator in a mixed-liquid medium, where each liquid has a different refractive index (typically ≈1–1.4) and is transparent in the microwave range, adjusting the concentration of the liquids allows for a gradual change in the effective refractive index n_{m} of the embedding medium, permitting continuous scanning over roughly half the desired octave, since the new frequency difference scales approximately as $\Delta fSn_{\mathrm{m}}/c$.

Within this range of axion masses and particle radii, we can proceed with the calculation of the respective transition rates. The transition matrix element for axion absorption from Eq. (15) [making use of Eqs. (1) and (2)] after some straightforward algebra

TABLE II. Axion mass, resonator size, and electromagnetic frequency correspondence.

Axion mass	Radius of the resonator	Frequency of EM radiation
1 eV/c^2	62.5 nm	ultraviolet band
1 meV/c^2	62.5 μm	terahertz band
1 μeV/c^2	62.5 mm	microwave band

becomes

$$G = \frac{\pi g_{\alpha\gamma\gamma}}{2}\int_V \mathrm{d}^3 r A(\mathbf{r})(\mathbf{E}^*_{E\ell m}(\mathbf{r};\omega_\mathrm{f})\cdot\mathbf{B}_{M\ell m}(\mathbf{r};\omega_\mathrm{i}) - \mathbf{B}^*_{E\ell m}(\mathbf{r};\omega_\mathrm{f})\cdot\mathbf{E}_{M\ell m}(\mathbf{r};\omega_\mathrm{i}))$$
$$= \frac{\pi g_{\alpha\gamma\gamma}A}{2}\sqrt{\epsilon\epsilon_0\mu\mu_0}a^*_{\mathrm{f};E\ell m}a_{\mathrm{i};M\ell m}I(\ell;S,q_\mathrm{i},q_\mathrm{f}), \tag{18}$$

where $I(\ell;S,q_\mathrm{i},q_\mathrm{f}) = \int_0^S r^2 dr[(\ell^2+\ell+1)\frac{j_\ell(q_\mathrm{i}r)j_\ell(q_\mathrm{f}r)}{q_\mathrm{i}q_\mathrm{f}r^2} + j'_\ell(q_\mathrm{i}r)j'_\ell(q_\mathrm{f}r) + j_\ell(q_\mathrm{i}r)j_\ell(q_\mathrm{f}r) + j'_\ell(q_\mathrm{i}r)\frac{j_\ell(q_\mathrm{f}r)}{q_\mathrm{f}r} + j'_\ell(q_\mathrm{f}r)\frac{j_\ell(q_\mathrm{i}r)}{q_\mathrm{i}r}]$. In Eq. (18), we assumed $A(\mathbf{r})$ to be homogeneous in the volume of the sphere, i.e., $A(\mathbf{r})\approx A$, since the de Broglie wavelength of the axion is very large (on the order of kilometers [32]). The coefficients $a_{\mathrm{i};M\ell m}$, $a_{\mathrm{f};E\ell m}$ can be calculated analytically with respect to the one-photon vacuum energy [67].

Now, we proceed to estimate the order of magnitude of the photon-to-photon transition rate mediated by galactic axions with mass $m_\alpha = 1\ \mu\mathrm{eV}/c^2$. For this mass, the radius of the spherical dielectric resonator must be set at 62.5 mm so that, for $\ell = 10$ the input $\mathrm{TE}_{\ell=10}$ resonates at 4.697 GHz ($\hbar\omega_\mathrm{i} = 1.943\times10^{-5}$ eV), while the output $\mathrm{TM}_{\ell=10}$ mode resonates at 4.939 GHz ($\hbar\omega_\mathrm{f} = 2.042\times10^{-5}$ eV). We set an indicative $|\tilde{g}_{\alpha\gamma\gamma}|$ on the order of $\sim10^{-13}$ GeV^{-1}. To compute the axion field amplitude $|A|$, we use the local dark matter density, typically taken to lie in the range $3\times10^{14}\lesssim\rho_{DM}\lesssim4\times10^{14}$ eV/m^3 [28,70,71,73], where we use the formula $|A| = \sqrt{2\rho_\mathrm{DM}\hbar^3}/c/m_\alpha$ from Ref. [73], which results in $|A|\simeq2.48\times10^3$ eV for $\rho_\mathrm{DM} = 4\times10^{14}$ eV/m^3. Based on these inputs, the prefactor $\frac{\pi}{2}\frac{|\tilde{g}_{\alpha\gamma\gamma}||A|}{\mu_0 c}\sqrt{\epsilon\epsilon_0\mu\mu_0}$ evaluates approximately 1.2×10^{-29} A s/(V m). The field amplitudes $|a_{\mathrm{i};M\ell m}|$, $|a_{\mathrm{i};E\ell m}|$ normalized to the one-photon vacuum energy [67] ($\frac{1}{4}\int_V(\epsilon\epsilon_0|E|^2+\frac{1}{\mu_0}|B|^2) = \hbar\omega_{\mathrm{i(f)}}$) of the initial and the final photon states, respectively, are found to be $|a_{\mathrm{i};M\ell m}| = 4.76\times10^{-5}$ V/m and $|a_{\mathrm{f};E\ell m}| = 5.10\times10^{-5}$ V/m. The radial integral yields $|I(\ell;S,q_\mathrm{i},q_\mathrm{f})| = 3.85\times10^{-7}$ m^3. Substituting all values into Eq. (18), we obtain a matrix element magnitude $|G|\simeq0.7\times10^{-25}$ eV. Applying Fermi's golden rule, i.e., $R_{\alpha\gamma\gamma} = \frac{2\pi}{\hbar}|G|^2\varrho(E_\mathrm{f})$ and using an optical density of states $\varrho(E_\mathrm{f})\simeq\frac{1}{\pi}\frac{2}{h\Gamma_\mathrm{f}}\simeq4.8\times10^8$ eV^{-1}, where $\Gamma_\mathrm{f}\simeq3.2\times10^{-4}$ GHz is the full width at half maximum of the final resonance (the quality factor is $Q_\mathrm{f}\simeq\frac{\hbar\omega_\mathrm{f}}{h\Gamma_\mathrm{f}}\simeq1.5\times10^4$), we find a photon-to-photon transition rate $R_{\alpha\gamma\gamma}\simeq0.2\times10^{-25}$ Hz. In practice, dielectric resonators are pumped with multiple photons, which accumulate in the cavity and enhance the transition probability. Assuming that the maximum sustainable electric field in silicon (that better corresponds to the given relative permittivity) is $E_\mathrm{max}\simeq3\times10^7$ V/m [95,96], the corresponding theoretical limit on the number of stored photons is $N\lesssim1.5\times10^{25}$ ($N = \frac{U_\mathrm{max}}{\hbar\omega_\mathrm{i}}$, where $U_\mathrm{max} = \frac{1}{2}\epsilon\epsilon_0\int_V|E_\mathrm{max}|^2 d\tau$ is the maximum stored energy inside the resonator). This leads to a maximum transition rate of $\tilde{R}_{\alpha\gamma\gamma} = N\times R_{\alpha\gamma\gamma}\simeq3.4\times10^{-2}$ Hz. The corresponding output power (photon energy × transition rate) $P_\mathrm{out} = (\hbar\omega_\mathrm{f})\times\tilde{R}_{\alpha\gamma\gamma}$ would be on the order of $\sim10^{-25}$ W, which is a theoretical upper limit for the given setup. However, in practice, the number of accumulated photons inside the cavity is determined by the input power P_in, the quality factor of the incoming resonance frequency Q_i and the corresponding frequency f_i, through the relation $N = P_\mathrm{in}Q_\mathrm{i}/2\pi hf_\mathrm{i}^2$. For a realistic continuous input power of $P_\mathrm{in} = 100$ W, the number of accumulated photons in the resonator will be $N\simeq2\times10^{19}$, where $Q_\mathrm{i}\simeq2\times10^4$. This results in output power on the order of $P_\mathrm{out}\sim10^{-30}$ W, which, although small, is not unusual of dark-matter searches.

To find ways for improving the output signal strength, we next investigate the scaling of P_out with the relevant intrinsic and external parameters of the system, paying particular attention to the scatterer size. In the upconversion approach, the first key step is to tailor the frequency splitting between the TE and TM modes so that it matches the unknown axion mass under investigation. As shown in Fig. 4(a), the separation $f_\mathrm{TM} - f_\mathrm{TE}$ ($=m_\alpha c^2/h$) can be continuously tuned by varying the sphere radius S, thereby selecting a specific target axion mass window at fixed material parameters. Although Fig. 4(a) shows only the representative case $\ell = 10$, the same inverse-radius trend ($m_\alpha\propto S^{-1}$) persists for higher-order Mie modes. Quantitatively, within the asymptotic description

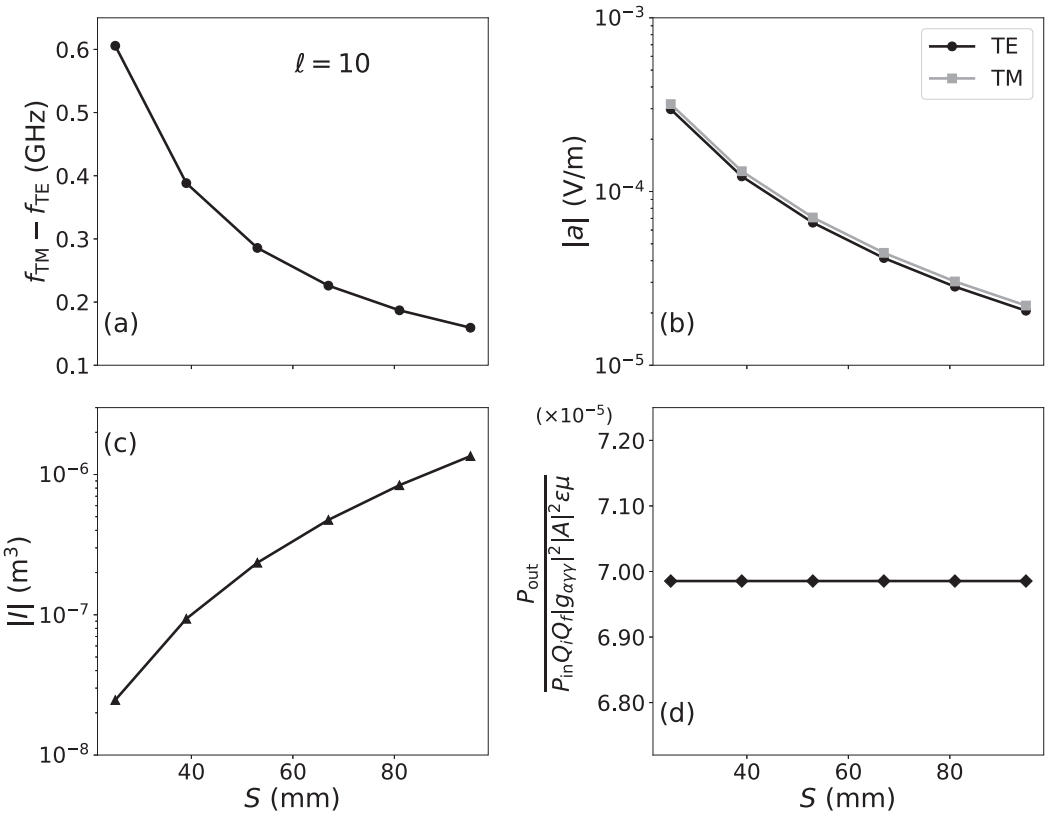


FIG. 4. (a) Frequency difference between TM and TE Mie modes, $f_{TM} - f_{TE}$, for angular momentum $\ell = 10$ as a function of the sphere radius S. The secondary vertical axis indicates the equivalent axion mass m_α ($\mu eV/c^2$) corresponding to the mode splitting. (b) Magnitude of the corresponding modal amplitudes $|a|$ for TE and TM modes, showing comparable scaling behavior with increasing S. (c) Absolute value of the overlap integral $|I|$ entering the transition matrix element, exhibiting a monotonic increase with the resonator size. (d) Normalized output power $P_{out}/[P_{in}Q_iQ_f|g_{a\gamma\gamma}|^2|A|^2\epsilon\mu]$ (dimensionless quantity), which remains approximately constant across the considered range of S.

[59], the TE-TM frequency splitting at $S = 25$ mm decreases from about 0.59 GHz for $\ell = 10$ to about 0.54 GHz for $\ell = 100$. At $S = 95$ mm, the corresponding values are approximately 0.155 and 0.142 GHz, respectively. Thus, increasing ℓ up to $\ell = 100$ produces only a modest reduction of the TE-TM splitting, while the dominant dependence remains the inverse scaling with the sphere radius. The other two panels of Fig. 4 clarify how the relevant photon-cavity quantities entering the transition matrix element G evolve with S. Panel (b) shows that the one-photon field amplitudes of the TE and TM modes of the same ℓ remain of comparable magnitude and decrease similarly with increasing radius. Panel (c) shows that the radial overlap integral $|I|$, which quantifies the spatial overlap between the initial and final resonant modes in Eq. (18), increases monotonically with S. Now, we express the output power P_{out} extracted from the spherical dielectric resonator in terms of the phenomenological parameters, in order to elucidate how it scales with the relevant cavity characteristics:

$$\frac{P_{out}}{P_{in}Q_iQ_f|\tilde{g}_{a\gamma\gamma}/(\mu_0 c)|^2|A|^2\epsilon\mu} = \pi^2 \frac{|a_{TM}|^2|a_{TE}|^2|I|^2}{(hf_i)^2}\epsilon_0\mu_0. \tag{19}$$

The right-hand side of Eq. (19) remains nearly constant under radius variation, as shown in Fig. 4(d). The weak variation observed in Fig. 4(d) indicates that, for the spherical Mie modes considered here, the photon-cavity characteristics (including the quality factors, which are independent of S) remain practically unaffected by the size of the spherical resonator. This provides the freedom to target different axion masses by varying the radius S without significantly altering the cavity-dependent contribution to the output power, apart from limitations imposed by the material breakdown threshold. We note, however, that the axion field amplitude $|A|$ is not strictly independent of S. Since $|A| \propto m_\alpha^{-1/2}$ and the resonant condition implies approximately $m_\alpha \propto S^{-1}$ [see Fig. 4(a)], we find $|A|^2 \propto S$. Therefore, while the factor shown in Fig. 4(d) remains essentially unchanged, the absolute output power acquires an additional approximately linear dependence on the resonator radius through the axion field amplitude. We now define the quantity $\frac{P_{\text{out}}}{P_{\text{in}}|\tilde{g}_{a\gamma\gamma}|^2|A|^2} \equiv C(\ell)$, which depends only on ℓ. Mathematically, according to the asymptotic relations [59], the parameter $C(\ell)$ grows with ℓ approximately as $C(\ell) \propto \ell^4$, indicating a preference for modes with higher ℓ due to their higher quality factors. Nevertheless, in physically realizable systems, this enhancement cannot be pursued indefinitely. Practical considerations, including material losses, finite axion coherence time, and other physical constraints, impose an upper limit on the usable cavity quality factors, as will be discussed later on.

To further enhance the sensitivity limit within the proposed physical framework, several advanced techniques can be explored, pushing the boundaries of current technological capabilities. Whispering gallery modes that are photonic resonances with high angular momentum indices ℓ, can achieve Q factors on the order of $\sim 10^5$–10^{10} [60–65]. From a practical standpoint, in whispering-gallery modes the excitation is naturally dominated by modes with $|m| = \ell$ [63,88], which are concentrated near the surface of the sphere, so the requirement $\delta_{mm'}$ is automatically satisfied, while the spectral separation between TE and TM WGMs with the same indices can be predicted analytically [59] despite the richness of the spectrum. If we assume, as a moderate case, $\ell = 14$, then the mathematical values of our lossless-cavity quality factors grow to $Q \sim 10^{10}$. This improvement would significantly increase the optical density of states $\varrho(E_{\text{f}})$ by additional orders of magnitude. However, when the resonator quality factor exceeds the axion field's intrinsic quality factor ($Q_\alpha \sim 10^6$), the effective enhancement of the optical density of states becomes limited by Q_α, and further increments do not contribute additional enhancement of $R_{\alpha\gamma\gamma}$. By taking this into account, the mathematical value of the parameter $C(\ell)$ is enhanced by a factor $\sim 10^7$. Furthermore, materials such as silicon carbide and fused silica or diamond that have low intrinsic losses and can handle higher electric fields than silicon by 1 and 2 orders of magnitude, respectively [95,97], are capable of sustaining larger numbers of photons ($N \sim 10^{27}$–10^{29}) without breaking down. We note however that refractive-index nonlinearities may occur at high field intensities, introducing additional noise into the measured signal. Therefore, materials such as diamond, which possess exceptionally high thresholds for nonlinear effects, may be preferable. To efficiently pump more photons inside the cavity, advanced pumping technologies such as Klystrons could be explored to provide the necessary energy and maximize the number of photons N. As today's Klystrons can provide orders of magnitude higher input power to the resonator, than the $P_{\text{in}} = 100\,\text{W}$ assumed before, a direction for future efforts would be to mitigate overheating while increasing the input power, with strategies such as pulsed pump operation as well as the development of thermal management techniques, to approach the theoretical upper limit of detectability. As an optimistic example, $P_{\text{in}} = 10\,\text{kW}$ on a diamond resonator at a cryogenic environment would increase the output power by a factor $\sim 10^2$. These two improvements, combined, could substantially increase the output power previously calculated by an order $\sim 10^9$, resulting in $P_{\text{out}} \sim 10^{-21}\,\text{W}$, a level within reach of state-of-the-art cryogenic microwave receivers.

The signal-to-noise ratio (SNR) in a haloscope-type search is governed by the Dicke radiometer equation

$$\text{SNR} = \frac{P_{\text{out}}}{k_B T_{\text{sys}}} \sqrt{\frac{t_{\text{int}}}{w}}, \tag{20}$$

where k_B is the Boltzmann's constant, $T_{\rm sys}$ the total system noise temperature (including all thermal, quantum, and detector contributions), w the detection bandwidth, and $t_{\rm int}$ the integration time per frequency step. For a cryogenic receiver with $T_{\rm sys} \simeq 5\,\mathrm{K}$ and $w \simeq 1\,\mathrm{Hz}$, it is $P_{\rm out}/(k_B T_{\rm sys}) \simeq 14.5$. Requiring a target sensitivity of SNR $\simeq 5$ yields $t_{\rm int} = (5/14.5)^2 \simeq 1.2 \times 10^{-1}$ s. Thus, an SNR of order 5 can be achieved with an integration time of approximately $t_{\rm int} \sim 0.1\,\mathrm{s}$ per frequency step. The expected axion signal bandwidth is $\Delta f_\alpha \sim f_\alpha/Q_\alpha$. For an axion mass $m_\alpha = 1\ \mu\mathrm{eV}/c^2$, the corresponding axion frequency is $f_\alpha = m_\alpha c^2/h \simeq 2.4 \times 10^8$ Hz, giving $\Delta f_\alpha \sim 2.4 \times 10^2$ Hz. Choosing the scan step size to be comparable to the axion linewidth, $\Delta f_{\rm step} \simeq \Delta f_\alpha$, corresponds to an effective scan quality factor $Q_{\rm scan} \equiv f_\alpha/\Delta f_{\rm step} \sim Q_\alpha \sim 10^6$. The number of frequency steps required to cover one octave (a factor-of-2span in axion frequency) is therefore $N_{\rm steps} \simeq Q_{\rm scan} \ln 2 \simeq 7 \times 10^5$. With $t_{\rm int} \simeq 0.12\,\mathrm{s}$ per step, the corresponding scan time is $T_{\rm oct} = N_{\rm steps} t_{\rm int} \approx 23$ h. Consequently, an octave in frequency can be scanned in approximately one day under these assumptions. We should also keep in mind that different sphere sizes allow parallel searches. Finally, we note that recent progress in superconducting microwave single-photon detectors operating at gigahertz frequencies [98–101] suggests an alternative, fully digital readout scheme, in which the SNR is governed by photon-counting statistics rather than by an effective noise temperature. Such devices have demonstrated rapid advances in sensitivity and may eventually provide a complementary route toward the detection of extremely weak axion-induced signals. Nevertheless, their deployment in a broadband, long-term axion haloscope search remains technologically more challenging than the cryogenic linear-receiver approach adopted here.

Moving to higher axion masses, for instance to $m_\alpha = 1\ \mathrm{meV}/c^2$, the characteristic frequency of the signal is pushed into the terahertz regime and the effective mode volume of the dielectric resonator is correspondingly reduced ($S = 62.5$ μm—see Table II). In this frequency range, the situation is qualitatively different from the microwave case discussed above: single-photon detection technology in the infrared and terahertz domains is substantially more mature, offering high quantum efficiencies and low dark-count rates. It is therefore natural, at these higher axion masses, to abandon the purely radiometric readout paradigm and to consider instead a photon-counting detection scheme. We note, however, that reducing the resonator radius to $S = 62.5$ μm decreases $|A|^2$ by a factor of 10^{-3}, as discussed earlier. Since $P_{\rm out} \propto |\tilde{g}_{\alpha\gamma\gamma}|^2 |A|^2$, the same output power can be retained by increasing the coupling constant $|\tilde{g}_{\alpha\gamma\gamma}|$ by a factor of $\sqrt{10^3}$. Thus, instead of $|\tilde{g}_{\alpha\gamma\gamma}| = 10^{-14}\ \mathrm{GeV}^{-1}$, we use $|\tilde{g}_{\alpha\gamma\gamma}| \simeq 3.16 \times 10^{-13}\ \mathrm{GeV}^{-1}$ for this higher-mass reference case. In this estimate, the previously assumed input power should be understood as an optimistic peak pulsed power rather than as a continuous-wave input power for a micron-scale dielectric resonator. For a single-photon detector with overall efficiency η and dark-count rate $R_{\rm dark}$, the number of detected signal photons in an integration time $t_{\rm int}$ is $N_{\rm sig} = \eta P_{\rm out} t_{\rm int}/(h f_0)$, while the background contribution is $N_{\rm dark} = R_{\rm dark} t_{\rm int}$. The corresponding signal-to-noise ratio is

$$\mathrm{SNR} = \frac{N_{\rm sig}}{\sqrt{N_{\rm sig} + N_{\rm dark}}}. \tag{21}$$

In the ideal shot-noise limit ($N_{\rm sig} \gg N_{\rm dark}$), we obtain $t_{\rm int}^{(\rm shot)} = \mathrm{SNR}^2 h f_0/(\eta P_{\rm out})$. For representative values $f_0 \simeq 5$ THz, $\eta \simeq 0.5$, $P_{\rm out} = 10^{-21}$ W, and a target SNR $\simeq 5$, this yields $t_{\rm int}^{(\rm shot)} \sim 170$ s per frequency step. For an axion mass $m_\alpha = 1\ \mathrm{meV}/c^2$, the corresponding axion frequency is $f_\alpha = m_\alpha c^2/h \simeq 2.4 \times 10^{11}$ Hz, giving $\Delta f_\alpha \sim 2.4 \times 10^5$ Hz. Choosing the scan step size $\Delta f_{\rm step} \simeq \Delta f_\alpha$ therefore corresponds to an effective scan quality factor $Q_{\rm scan} \equiv f_\alpha/\Delta f_{\rm step} \sim Q_\alpha \sim 10^6$. The number of independent frequency steps required to cover one octave is then $N_{\rm steps} \simeq Q_{\rm scan} \ln 2 \approx 7 \times 10^5$, and the total scan time $T_{\rm oct} = N_{\rm steps}\, t_{\rm int}^{(\rm shot)} \approx 3.7$ years. Including realistic dark counts in the dark-count-limited regime modifies the required integration time according to $t_{\rm int}^{(\rm dark)} = (\mathrm{SNR}\, h f_0/(\eta P_{\rm out}))^2 R_{\rm dark}$, which can lengthen $T_{\rm oct}$ further, depending on the achievable dark-count rate of the infrared/terahertz detector. However, parallel operation of multiple resonators could offer a path toward substantially accelerating the overall survey time. We also note that the proposed scheme achieves its maximum sensitivity under triply resonant conditions, with the enhancement

progressively diminishing as the detuning between the axion frequency and the cavity mode splitting exceeds the effective linewidth.

The above discussions correspond to an optimistic scenario illustrating the ultimate potential of the proposed framework. However, a more moderate and technologically conservative benchmark would be also instructive. Specifically, we now assume a similar implementation driven with a continuous input power of $P_{\rm in} = 100$ W and include a representative damping of the signal due to thermal losses in the resonator by assuming an effective quality factor $Q_{\rm eff} \simeq 10^{-1}Q$ for each resonant mode. Although such losses are expected to remain relatively small in low-loss dielectric materials operated at cryogenic temperatures, they reduce the achievable output power compared to the optimistic estimate. To facilitate a direct comparison with the optimistic scenario, we retain the same target sensitivity (SNR = 5), integration times, scan rates, and octave-scan durations. Under these assumptions, the corresponding couplings become $|\tilde{g}_{a\gamma\gamma}| \simeq 10^{-11}\,\mathrm{GeV}^{-1}$ at $m_a = 1\ \mu\mathrm{eV}/c^2$ and $|\tilde{g}_{a\gamma\gamma}| \simeq 3.16 \times 10^{-10}\,\mathrm{GeV}^{-1}$ at $m_a = 1\ \mathrm{meV}/c^2$. These values define a baseline scenario that may be regarded as a realistic first-generation implementation of a respective experiment, whereas the optimistic scenario marks the sensitivity that could become accessible through future improvements in resonator performance, thermal management, and drive technology.

A future experiment based on this framework could be named DARK-ROSE, which stands for DARK matter search via resonant optical scattering experiment. Figure 5 illustrates the projected DARK-ROSE sensitivity within the broader axion landscape. Existing exclusions from haloscopes (RBF + UF [102,103], ADMX [33–35]) and the helioscope CAST [41,42] delimit the currently probed parameter space, while the semitransparent gray-scale overlays indicate projected sensitivities from HAYSTAC [104] and TOORAD [28,29] (haloscopes), MADMAX [105] (dielectric haloscope), IAXO [43,44] (next-generation helioscope), and the UPLOAD-CMC-II-Cryo upconversion experiment [48], providing complementary (future) coverage across the $\mu\mathrm{eV}/c^2$ to meV/c^2 mass window. The rose-shaded DARK-ROSE region is obtained from the two benchmark calculations discussed above, namely, for $m_a = 1\ \mu\mathrm{eV}/c^2$ and for $m_a = 1\ \mathrm{meV}/c^2$, assuming a target sensitivity of SNR = 5. The corresponding dotted boundary in Fig. 5 represents the optimistic scenario based on cryogenic operation, high-Q resonators and peak excitation. The benchmark points defining the optimistic scenario are ($m_a = 1\ \mu\mathrm{eV}/c^2$, $|\tilde{g}_{a\gamma\gamma}| \simeq 10^{-14}\ \mathrm{GeV}^{-1}$) and ($m_a = 1\ \mathrm{meV}/c^2$, $|\tilde{g}_{a\gamma\gamma}| \simeq 3.16 \times 10^{-13}\ \mathrm{GeV}^{-1}$). The solid boundary denotes the baseline scenario, corresponding to a cryogenic 100 W implementation including representative losses. The benchmark points defining the baseline scenario are ($m_a = 1\ \mu\mathrm{eV}/c^2$, $|\tilde{g}_{a\gamma\gamma}| \simeq 10^{-11}\ \mathrm{GeV}^{-1}$) and ($m_a = 1\ \mathrm{meV}/c^2$, $|\tilde{g}_{a\gamma\gamma}| \simeq 3.16 \times 10^{-10}\ \mathrm{GeV}^{-1}$). Both scenarios assume identical integration times and scan rates, with the change in sensitivity arising solely from the adopted experimental parameters. The intermediate sensitivities are obtained from the scaling relations derived in this section. As shown in Fig. 5, DARK-ROSE probes a broad axionlike parameter space extending from the sub-μeV region toward the meV scale, overlapping part of the parameter space addressed by resonant upconversion searches while remaining complementary to conventional haloscope and helioscope techniques. Although the projected sensitivity does not reach the KSVZ and DFSZ QCD-axion bands, a future development could explore a region that is currently largely unconstrained and demonstrates the potential of resonantly enhanced axion-mediated photon-to-photon transitions as a novel search strategy. Additionally, our approach might assist the *shining through walls* [106–110] experiments, where strong laboratory-produced electromagnetic fields could generate axions (through the Primmakoff effect) that then pass through opaque barriers and be detected on the far side. Apart from the (dark matter) axions considered in this work, the underlying mechanism and theoretical framework may also be extended to encompass solid-state axions (axion quasiparticles). In particular, if the resonator material is chosen to be an antiferromagnetically doped topological insulator [28–30] or a bianisotropic [111–113]/Tellegen metamaterial [114–119], it can intrinsically support axionlike electromagnetic responses.

Finally, it is interesting to briefly comment on the potential of the spherical dielectric system proposed here, compared to the cylindrical metallic cavity used in the UPLOAD experiment [49], which is a mature technology. The UPLOAD experiment is an AC axion haloscope based on a

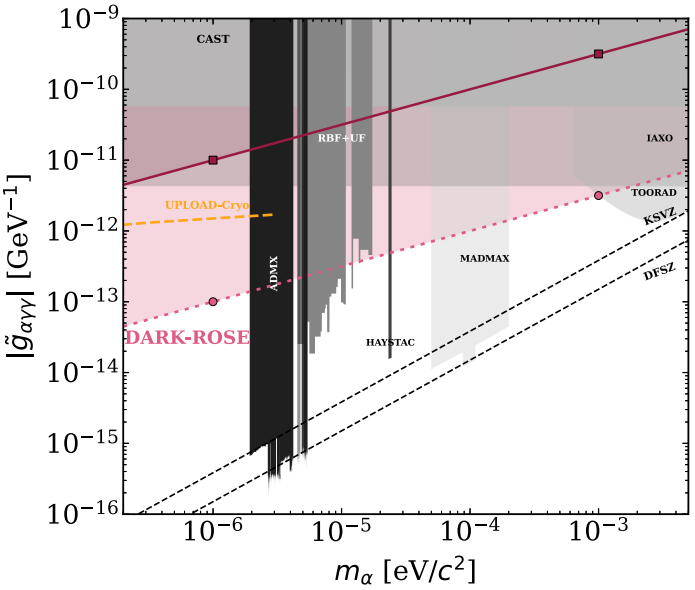


FIG. 5. Constraints and projected sensitivities on the axion-photon-photon coupling $|\tilde{g}_{a\gamma\gamma}|$ as a function of the axion mass m_a. The DARK-ROSE projections are obtained from the two benchmark calculations discussed in Sec. V ($m_\alpha = 1$ μeV/c^2 and $m_\alpha = 1$ meV/c^2), assuming SNR = 5. The dotted rose boundary corresponds to the optimistic scenario, while the solid dark-red boundary corresponds to a baseline scenario assuming a cryogenic 100 W implementation with representative losses included. For both scenarios, the benchmark sensitivities are defined using integration times $t_{\rm int} \approx 0.12$ s (for $m_\alpha = 1$ μeV/c^2) and $t_{\rm int} \approx 170$ s (for $m_\alpha = 1$ meV/c^2) per frequency step, for an axion coherence quality factor $Q_\alpha \simeq 10^6$. The intermediate and extrapolated DARK-ROSE sensitivities are obtained from the scaling relations derived in Sec. V. The dashed orange curve indicates the projected reach of the UPLOAD-II-Cryo upconversion experiment. Shaded regions correspond to existing exclusion limits from CAST, RBF + UF, and ADMX, while semitransparent gray-scale regions indicate the projected sensitivities of HAYSTAC, TOORAD, MADMAX, and IAXO (datasets obtained from the AxionLimits repository maintained by C. O'Hare). The dashed lines show the benchmark KSVZ and DFSZ QCD axion models. Both axes are logarithmic; the displayed parameter space covers 2×10^{-7} eV/$c^2 \leqslant m_a \leqslant 5 \times 10^{-3}$ eV/c^2 and 10^{-16} GeV$^{-1} \leqslant |\tilde{g}_{a\gamma\gamma}| \leqslant 10^{-9}$ GeV^{-1}.

cylindrical metallic cavity, where the axion-mediated photon upconversion is expected through different cylindrical eigenmodes. The sensitivity of the setup is determined by the so-called overlap functions $\xi_{ij} = \frac{1}{V}\int \mathbf{e}_i(\mathbf{r}) \cdot \mathbf{b}_j(\mathbf{r}) dV$, where $\mathbf{e}_{i,j}$ and $\mathbf{b}_{i,j}$ are the mode electric and magnetic field real unit vectors, such that $0 \leqslant \xi_{ij} \leqslant 1$. For the cylindrical case, one finds $\xi_{i,j} \simeq 0.4$–0.5 for an optimum mode pair selection (e.g., TE_{011}-TM_{020}) [49]. In contrast, for the spherical dielectric resonator considered here, the normalized electric and magnetic mode profiles of TE and TM multipoles of the same ℓ are everywhere parallel inside the resonator volume, as can be seen from Eqs. (1) and (2). In this case, the corresponding overlap reaches $\xi_{ij} = 1$ for any pair allowed by the selection rule. We emphasize that the overlap coefficients ξ_{ij} are defined in terms of normalized mode profiles and therefore quantify, in the present spherical geometry, only the angular overlap between the participating modes, while the radial dependence is entirely contained in the radial overlap integral $I(\ell; S; q_i, q_f)$. On the other hand, the matrix element G [Eq. (18)] for the spherical dielectric cavity is reduced by a factor $1/\sqrt{\epsilon}$ compared to a perfectly electric conducting (PEC) spherical cavity of the same radius. The respective eigenmodes of the PEC spherical cavity have the same structure as Eqs. (1) and (2) but without the $\sqrt{\epsilon\mu}$ factor, and their discrete wave numbers are fixed by the PEC boundary conditions [52]. When the fields are normalized to the one-photon vacuum energy, the photon field amplitudes in the dielectric sphere acquire an additional factor of $1/\sqrt{\epsilon}$, with respect to

the PEC ones. These prefactors combined are responsible for the net $1/\sqrt{\epsilon}$ reduction of the matrix element G of the dielectric sphere compared to the PEC one. Overall, the spherical dielectric cavity offers maximal geometric overlap ($\xi_{ij} = 1$) but a reduced matrix element $G \propto 1/\sqrt{\epsilon}$, with respect to a PEC spherical cavity of the same volume, whereas the cylindrical metallic UPLOAD cavity has smaller overlap ($\xi_{ij} \sim 0.5$) but benefits from the larger photon field amplitudes of a PEC resonator.

VI. CONCLUSIONS

To summarize, we investigated (dark matter) axion-mediated photonic transitions within a spherical, high-finesse dielectric resonator and derived the corresponding selection rule based on group theory. Using the first-order Born approximation, we analytically computed the enhancement of the transition rates associated with axion absorption and emission processes. The analytic scalings identify experimentally accessible regimes, including millimeter-scale spheres at microwave frequencies, and suggest scan strategies via the resonator size and the embedding medium refractive index. Importantly, the scheme operates without an external magnetic field. These findings could have direct implications for the design of resonant axion devices. Moreover, the underlying framework may also inspire future applications in engineered axionlike quasiparticle dynamics in electromagnetic metamaterials.

DATA AVAILABILITY

All results were obtained through analytical calculations and can be independently reproduced.

[1] V. C. Rubin and W. K. Ford, Jr., Rotation of the Andromeda Nebula from a spectroscopic survey of emission regions, Astrophys. J. **159**, 379 (1970).

[2] S. Heinemeyer, M. Mondragon, and G. Zoupanos, Confronting finite unified theories with low-energy phenomenology, J. High Energy Phys. 07 (2008) 135.

[3] G. Bertone and D. Hooper, History of dark matter, Rev. Mod. Phys. **90**, 045002 (2018).

[4] D. F. Jackson Kimball and K. Van Bibber, *The Search for Ultralight Bosonic Dark Matter* (Springer Nature, 2023).

[5] W. DeRocco, M. Galanis, and R. Lasenby, Dark matter scattering in astrophysical media: Collective effects, J. Cosmol. Astropart. Phys. 05 (2022) 015.

[6] K. Choi, S. H. Im, and C. S. Shin, Recent progress in the physics of axions and axion-like particles, Annu. Rev. Nucl. Part. Sci. **71**, 225 (2021).

[7] J. E. Kim and G. Carosi, Axions and the strong CP problem, Rev. Mod. Phys. **82**, 557 (2010).

[8] C. Adams, N. Aggarwal, A. Agrawal, R. Balafendiev, C. Bartram, M. Baryakhtar, H. Bekker, P. Belov, K. Berggren, A. Berlin, *et al.*, Axion dark matter, arXiv:2203.14923.

[9] R. D. Peccei and H. R. Quinn, CP conservation in the presence of pseudoparticles, Phys. Rev. Lett. **38**, 1440 (1977).

[10] F. Wilczek, Problem of strong P and T invariance in the presence of instantons, Phys. Rev. Lett. **40**, 279 (1978).

[11] S. Weinberg, A new light boson? Phys. Rev. Lett. **40**, 223 (1978).

[12] C. Coriano, N. Irges, and S. Morelli, Stückelberg axions and the effective action of anomalous Abelian models 1. A unitarity analysis of the Higgs-axion mixing, J. High Energy Phys. 07 (2007) 008.

[13] E. Masso and J. Redondo, Evading astrophysical constraints on axion-like particles, J. Cosmol. Astropart. Phys. 09 (2005) 015.

[14] M. D. Marsh, H. R. Russell, A. C. Fabian, B. R. McNamara, P. Nulsen, and C. S. Reynolds, A new bound on axion-like particles, J. Cosmol. Astropart. Phys. 12 (2017) 036.

[15] I. G. Irastorza and J. Redondo, New experimental approaches in the search for axion-like particles, Prog. Part. Nucl. Phys. **102**, 89 (2018).
[16] V. Desjacques, A. Kehagias, and A. Riotto, Impact of ultralight axion self-interactions on the large scale structure of the universe, Phys. Rev. D **97**, 023529 (2018).
[17] A. Arvanitaki, S. Dimopoulos, M. Galanis, L. Lehner, J. O. Thompson, and K. Van Tilburg, Large-misalignment mechanism for the formation of compact axion structures: Signatures from the QCD axion to fuzzy dark matter, Phys. Rev. D **101**, 083014 (2020).
[18] N. E. Mavromatos, V. C. Spanos, and I. D. Stamou, Primordial black holes and gravitational waves in multiaxion-Chern-Simons inflation, Phys. Rev. D **106**, 063532 (2022).
[19] S. Alexander, T. Manton, and E. McDonough, Field theory axiverse, Phys. Rev. D **109**, 116019 (2024).
[20] B. D. Tellegen, The gyrator, a new electric network element, Philips Res. Rep. **3**, 81 (1948).
[21] L. D. Landau and E. M. Lífshíts, *Electrodynamics of Continuous Media* (Pergamon Press, Oxford, 1960), Vol. 2.
[22] I. E. Dzyaloshinskii, On the magneto-electrical effects in antiferromagnets, Sov. Phys. JETP **10**, 628 (1960).
[23] B. Krichevtsov, V. Pavlov, R. Pisarev, and V. Gridnev, Spontaneous non-reciprocal reflection of light from antiferromagnetic Cr_2O_3, J. Phys.: Condens. Matter **5**, 8233 (1993).
[24] L. Wu, M. Salehi, N. Koirala, J. Moon, S. Oh, and N. Armitage, Quantized Faraday and Kerr rotation and axion electrodynamics of a 3D topological insulator, Science **354**, 1124 (2016).
[25] V. Dziom, A. Shuvaev, A. Pimenov, G. Astakhov, C. Ames, K. Bendias, J. Böttcher, G. Tkachov, E. Hankiewicz, C. Brüne, *et al.*, Observation of the universal magnetoelectric effect in a 3D topological insulator, Nat. Commun. **8**, 15197 (2017).
[26] N. Varnava and D. Vanderbilt, Surfaces of axion insulators, Phys. Rev. B **98**, 245117 (2018).
[27] T. Z. Seidov and M. A. Gorlach, Hybridization of electric and magnetic responses in the effective axion background, Phys. Rev. A **108**, 053515 (2023).
[28] D. J. Marsh, K. C. Fong, E. W. Lentz, L. Šmejkal, and M. N. Ali, Proposal to detect dark matter using axionic topological antiferromagnets, Phys. Rev. Lett. **123**, 121601 (2019).
[29] J. Schütte-Engel, D. J. Marsh, A. J. Millar, A. Sekine, F. Chadha-Day, S. Hoof, M. N. Ali, K. C. Fong, E. Hardy, and L. Šmejkal, Axion quasiparticles for axion dark matter detection, J. Cosmol. Astropart. Phys. 08 (2021) 066.
[30] A. Esposito and S. Pavaskar, Optimal antiferromagnets for light dark matter detection, Phys. Rev. D **108**, L011901 (2023).
[31] P. G. Catinari, A. Esposito, and S. Pavaskar, Hunting axion dark matter with antiferromagnets: A case study with nickel oxide, Phys. Rev. D **112**, 035007 (2025).
[32] Y. K. Semertzidis and S. Youn, Axion dark matter: How to see it? Sci. Adv. **8**, eabm9928 (2022).
[33] T. Nitta, T. Braine, N. Du, M. Guzzetti, C. Hanretty, G. Leum, L. Rosenberg, G. Rybka, J. Sinnis, J. Clarke, *et al.*, Search for a dark-matter-induced cosmic axion background with ADMX, Phys. Rev. Lett. **131**, 101002 (2023).
[34] B. T. McAllister, A. P. Quiskamp, and M. E. Tobar, Tunable rectangular resonant cavities for axion haloscopes, Phys. Rev. D **109**, 015013 (2024).
[35] G. Carosi, C. Cisneros, N. Du, S. Durham, N. Robertson, C. Goodman, M. Guzzetti, C. Hanretty, K. Enzian, L. Rosenberg, *et al.*, Search for axion dark matter from 1.1 to 1.3 GHz with ADMX, Phys. Rev. Lett. **135**, 191001 (2025).
[36] A. J. Millar, G. G. Raffelt, J. Redondo, and F. D. Steffen, Dielectric haloscopes to search for axion dark matter: Theoretical foundations, J. Cosmol. Astropart. Phys. 01 (2017) 061.
[37] A. Caldwell, G. Dvali, B. Majorovits, A. Millar, G. Raffelt, J. Redondo, O. Reimann, F. Simon, F. Steffen, *et al.* (MADMAX Working Group), Dielectric haloscopes: A new way to detect axion dark matter, Phys. Rev. Lett. **118**, 091801 (2017).
[38] H. Terças, J. Rodrigues, and J. Mendonça, Axion-plasmon polaritons in strongly magnetized plasmas, Phys. Rev. Lett. **120**, 181803 (2018).
[39] M. Lawson, A. J. Millar, M. Pancaldi, E. Vitagliano, and F. Wilczek, Tunable axion plasma haloscopes, Phys. Rev. Lett. **123**, 141802 (2019).

[40] A. J. Millar, S. M. Anlage, R. Balafendiev, P. Belov, K. Van Bibber, J. Conrad, M. Demarteau, A. Droster, K. Dunne, A. G. Rosso, *et al.*, Searching for dark matter with plasma haloscopes, Phys. Rev. D **107**, 055013 (2023).

[41] K. Zioutas, S. Andriamonje, V. Arsov, S. Aune, D. Autiero, F. Avignone, K. Barth, A. Belov, B. Beltrán, H. Bräuninger, *et al.*, First results from the CERN Axion Solar Telescope, Phys. Rev. Lett. **94**, 121301 (2005).

[42] E. Arik, S. Aune, D. Autiero, K. Barth, A. Belov, B. Beltrán, S. Borghi, G. Bourlis, F. Boydag, H. Bräuninger, *et al.*, Probing eV-scale axions with CAST, J. Cosmol. Astropart. Phys. 02 (2009) 008.

[43] E. Armengaud, F. Avignone, M. Betz, P. Brax, P. Brun, G. Cantatore, J. Carmona, G. Carosi, F. Caspers, S. Caspi, *et al.*, Conceptual design of the International Axion Observatory (IAXO), J. Instrum. **9**, T05002 (2014).

[44] E. Armengaud, D. Attié, S. Basso, P. Brun, N. Bykovskiy, J. Carmona, J. Castel, S. Cebrián, M. Cicoli, M. Civitani, *et al.*, Physics potential of the International Axion Observatory (IAXO), J. Cosmol. Astropart. Phys. 06 (2019) 047.

[45] G. Galanti and M. Roncadelli, Axion-like particles implications for high-energy astrophysics, Universe **8**, 253 (2022).

[46] C. Murgui, Y. Wang, and K. M. Zurek, Axion detection with optomechanical cavities, Phys. Lett. B **855**, 138832 (2024).

[47] A. Berlin, R. T. D'Agnolo, S. A. R. Ellis, C. Nantista, J. Neilson, P. Schuster, S. Tantawi, N. Toro, and K. Zhou, Axion dark matter detection by superconducting resonant frequency conversion, J. High Energy Phys. 07 (2020) 088.

[48] C. A. Thomson, B. T. McAllister, M. Goryachev, E. N. Ivanov, and M. E. Tobar, Upconversion loop oscillator axion detection experiment: A precision frequency interferometric axion dark matter search with a cylindrical microwave cavity, Phys. Rev. Lett. **126**, 081803 (2021).

[49] C. A. Thomson, M. Goryachev, B. T. McAllister, E. N. Ivanov, P. Altin, and M. E. Tobar, Searching for low-mass axions using resonant upconversion, Phys. Rev. D **107**, 112003 (2023).

[50] G. Mie, Beiträge zur optik trüber medien, speziell kolloidaler metallösungen, Ann. Phys. **330**, 377 (1908).

[51] C. F. Bohren and D. R. Huffman, *Absorption and Scattering of Light by Small Particles* (John Wiley & Sons, 2008).

[52] J. D. Jackson, *Classical Electrodynamics* (John Wiley & Sons, 2021).

[53] R. Fenollosa, F. Ramiro-Manzano, M. Garín, and F. Meseguer, Silicon microspheres for super-Planckian light sources in the mid infrared, Adv. Opt. Mater. **11**, 2300135 (2023).

[54] O. Mitrofanov, F. Dominec, P. Kužel, J. L. Reno, I. Brener, U.-C. Chung, C. Elissalde, M. Maglione, and P. Mounaix, Near-field probing of Mie resonances in single TiO_2 microspheres at terahertz frequencies, Opt. Express **22**, 23034 (2014).

[55] B. Lukyanchuk, L. M. Vasilyak, V. Ya. Pecherkin, S. P. Vetchinin, V. E. Fortov, Z. B. Wang, R. Paniagua-Domínguez, and A. A. Fedyanin, Colossal magnetic fields in high refractive index materials at microwave frequencies, Sci. Rep. **11**, 23453 (2021).

[56] U. Dey, J. G. Marin, and J. Hesselbarth, Low-loss and tunable millimeter-wave filters using spherical dielectric resonators, Int. J. Microw. Wireless Technol. **13**, 751 (2021).

[57] A. Subrahmannian, V. S. Yadav, A. Patnaik, and U. Dey, On the study of fundamental modes of spherical dielectric resonator at millimeter-wave frequency, in *2022 IEEE Microwaves, Antennas, and Propagation Conference (MAPCON)* (IEEE, 2022), pp. 231–236.

[58] A. Galante, A. Contestabile, A. Capocefalo, V. Galdi, C. Rizza, and M. Alecci, Observation of radio-frequency Mie resonances in high-permittivity dielectric spheres, J. Phys. D: Appl. Phys. **58**, 135122 (2025).

[59] C. C. Lam, P. T. Leung, and K. Young, Explicit asymptotic formulas for the positions, widths, and strengths of resonances in Mie scattering, J. Opt. Soc. Am. B **9**, 1585 (1992).

[60] M. L. Gorodetsky, A. A. Savchenkov, and V. S. Ilchenko, Ultimate Q of optical microsphere resonators, Opt. Lett. **21**, 453 (1996).

[61] L. Yu and V. Fernicola, Spherical-sapphire-based whispering gallery mode resonator thermometer, Rev. Sci. Instrum. **83**, 094903 (2012).
[62] A. Rueda, F. Sedlmeir, M. C. Collodo, U. Vogl, B. Stiller, G. Schunk, D. V. Strekalov, C. Marquardt, J. M. Fink, O. Painter, *et al.*, Efficient microwave to optical photon conversion: An electro-optical realization, Optica **3**, 597 (2016).
[63] D. W. Vogt and R. Leonhardt, Ultra-high Q terahertz whispering-gallery modes in a silicon resonator, APL Photonics **3**, 051702 (2018).
[64] N. J. Lambert, A. Rueda, F. Sedlmeir, and H. G. L. Schwefel, Coherent conversion between microwave and optical photons—An overview of physical implementations, Adv. Quantum Technol. **3**, 1900077 (2020).
[65] V. S. Ilchenko, A. M. Bennett, P. Santini, A. A. Savchenkov, A. B. Matsko, and L. Maleki, Whispering gallery mode diamond resonator, Opt. Lett. **38**, 4320 (2013).
[66] N. Stefanou, V. Yannopapas, and A. Modinos, Heterostructures of photonic crystals: Frequency bands and transmission coefficients, Comput. Phys. Commun. **113**, 49 (1998).
[67] E. Almpanis, G. Zouros, P. Pantazopoulos, K. Tsakmakidis, N. Papanikolaou, and N. Stefanou, Spherical optomagnonic microresonators: Triple-resonant photon transitions between Zeeman-split Mie modes, Phys. Rev. B **101**, 054412 (2020).
[68] E. Almpanis, G. P. Zouros, and N. Papanikolaou, Spherical optomagnonic resonators, in *Optomagnonic Structures: Novel Architectures for Simultaneous Control of Light and Spin Waves*, edited by E. Almpanis (World Scientific, 2021), pp. 243–297.
[69] G. Gantzounis, Plasmon modes of axisymmetric metallic nanoparticles: A group theory analysis, J. Phys. Chem. C **113**, 21560 (2009).
[70] H. S. Røising, B. Fraser, S. M. Griffin, S. Bandyopadhyay, A. Mahabir, S.-W. Cheong, and A. V. Balatsky, Axion-matter coupling in multiferroics, Phys. Rev. Res. **3**, 033236 (2021).
[71] A. Berlin and T. Trickle, Absorption of axion dark matter in a magnetized medium, Phys. Rev. Lett. **132**, 181801 (2024).
[72] P. Sikivie, Experimental tests of the "invisible" axion, Phys. Rev. Lett. **51**, 1415 (1983).
[73] Y. Kim, D. Kim, J. Jeong, J. Kim, Y. C. Shin, and Y. K. Semertzidis, Effective approximation of electromagnetism for axion haloscope searches, Phys. Dark Universe **26**, 100362 (2019).
[74] P. Sikivie, Axion dark matter, Nucl. Phys. B **1003**, 116500 (2024).
[75] L. Visinelli, Axion-electromagnetic waves, Mod. Phys. Lett. A **28**, 1350162 (2013).
[76] I. Brevik, Axion electrodynamics and the axionic Casimir effect, Universe **7**, 133 (2021).
[77] D. J. Griffiths, *Introduction to Electrodynamics* (Cambridge University Press, 2023).
[78] F. Wilczek, Two applications of axion electrodynamics, Phys. Rev. Lett. **58**, 1799 (1987).
[79] S. Chigusa, T. Moroi, and K. Nakayama, Detecting light boson dark matter through conversion into a magnon, Phys. Rev. D **101**, 096013 (2020).
[80] M. S. Turner, Periodic signatures for the detection of cosmic axions, Phys. Rev. D **42**, 3572 (1990).
[81] P. W. Graham, I. G. Irastorza, S. K. Lamoreaux, A. Lindner, and K. A. van Bibber, Experimental searches for the axion and axion-like particles, Annu. Rev. Nucl. Part. Sci. **65**, 485 (2015).
[82] A. Quiskamp, B. T. McAllister, P. Altin, E. N. Ivanov, M. Goryachev, and M. E. Tobar, Direct search for dark matter axions excluding ALP cogenesis in the 63- to 67-μeV range with the ORGAN experiment, Sci. Adv. **8**, eabq3765 (2022).
[83] C. Wolff, M. Smith, B. Stiller, and C. Poulton, Brillouin scattering—Theory and experiment: Tutorial, J. Opt. Soc. Am. B **38**, 1243 (2021).
[84] G. Gantzounis, N. Papanikolaou, and N. Stefanou, Nonlinear interactions between high-Q optical and acoustic modes in dielectric particles, Phys. Rev. B **84**, 104303 (2011).
[85] E. Almpanis, Dielectric magnetic microparticles as photomagnonic cavities: Enhancing the modulation of near-infrared light by spin waves, Phys. Rev. B **97**, 184406 (2018).
[86] I. Stefanou, P. A. Pantazopoulos, and N. Stefanou, Light scattering by a spherical particle with a time-periodic refractive index, J. Opt. Soc. Am. B **38**, 407 (2021).

[87] E. Panagiotidis, E. Almpanis, N. Papanikolaou, and N. Stefanou, Inelastic light scattering from a dielectric sphere with a time-varying radius, Phys. Rev. A **106**, 013524 (2022).
[88] J. Haigh, A. Nunnenkamp, A. Ramsay, and A. Ferguson, Triple-resonant Brillouin light scattering in magneto-optical cavities, Phys. Rev. Lett. **117**, 133602 (2016).
[89] X. Zhang, N. Zhu, C.-L. Zou, and H. X. Tang, Optomagnonic whispering gallery microresonators, Phys. Rev. Lett. **117**, 123605 (2016).
[90] A. Osada, R. Hisatomi, A. Noguchi, Y. Tabuchi, R. Yamazaki, K. Usami, M. Sadgrove, R. Yalla, M. Nomura, and Y. Nakamura, Cavity optomagnonics with spin-orbit coupled photons, Phys. Rev. Lett. **116**, 223601 (2016).
[91] E. Panagiotidis, E. Almpanis, N. Papanikolaou, and N. Stefanou, Optical transitions and nonreciprocity in spatio-temporally periodic layers of spherical particles, Adv. Opt. Mater. **11**, 2202812 (2023).
[92] P. Sikivie, Axion dark matter detection using atomic transitions, Phys. Rev. Lett. **113**, 201301 (2014).
[93] M. I. Mishchenko, L. D. Travis, and A. A. Lacis, *Scattering, Absorption, and Emission of Light by Small Particles* (Cambridge University Press, 2002).
[94] J.-M. Geffrin, B. García-Cámara, R. Gómez-Medina, P. Albella, L. Froufe-Pérez, C. Eyraud, A. Litman, R. Vaillon, F. González, M. Nieto-Vesperinas, *et al.*, Magnetic and electric coherence in forward- and back-scattered electromagnetic waves by a single dielectric subwavelength sphere, Nat. Commun. **3**, 1171 (2012).
[95] R. Singh, Reliability and performance limitations in SiC power devices, Microelectron. Reliab. **46**, 713 (2006).
[96] C. Kim and R. Ramprasad, Dielectric breakdown field of strained silicon under hydrostatic pressure, Appl. Phys. Lett. **111**, 112904 (2017).
[97] A. Denisenko and E. Kohn, Diamond power devices. Concepts and limits, Diamond Relat. Mater. **14**, 491 (2005).
[98] A. L. Pankratov, L. S. Revin, A. V. Gordeeva, A. A. Yablokov, L. S. Kuzmin, and E. Il'Ichev, Towards a microwave single-photon counter for searching axions, npj Quantum Inf. **8**, 61 (2022).
[99] L. Balembois, J. Travesedo, L. Pallegoix, A. May, E. Billaud, M. Villiers, D. Estève, D. Vion, P. Bertet, and E. Flurin, Cyclically operated microwave single-photon counter with sensitivity of 10^{-22} W/Hz, Phys. Rev. Appl. **21**, 014043 (2024).
[100] C. Braggio, L. Balembois, R. Di Vora, Z. Wang, J. Travesedo, L. Pallegoix, G. Carugno, A. Ortolan, G. Ruoso, U. Gambardella, *et al.*, Quantum-enhanced sensing of axion dark matter with a transmon-based single microwave photon counter, Phys. Rev. X **15**, 021031 (2025).
[101] T. Kim, Modeling and simulation of microwave kinetic inductance detector readout system using simulink and RF blockset, IEEE Trans. Appl. Supercond. **35**, 1400506 (2025).
[102] S. DePanfilis, A. C. Melissinos, B. E. Moskowitz, J. T. Rogers, Y. K. Semertzidis, W. U. Wuensch, H. J. Halama, A. G. Prodell, W. B. Fowler, and F. A. Nezrick, Limits on the abundance and coupling of cosmic axions at $4.5 < m_a < 5.0\,\mu$eV, Phys. Rev. Lett. **59**, 839 (1987).
[103] C. Hagmann, P. Sikivie, N. S. Sullivan, and D. B. Tanner, Results from a search for cosmic axions, Phys. Rev. D **42**, 1297 (1990).
[104] L. Zhong, S. Al Kenany, K. M. Backes, B. M. Brubaker, S. B. Cahn, G. Carosi, Y. V. Gurevich, W. F. Kindel, S. K. Lamoreaux, K. W. Lehnert, *et al.*, Results from phase 1 of the HAYSTAC microwave cavity axion experiment, Phys. Rev. D **97**, 092001 (2018).
[105] S. Beurthey, N. Böhmer, P. Brun, A. Caldwell, L. Chevalier, C. Diaconu, G. Dvali, P. Freire, E. Garutti, C. Gooch, *et al.*, MADMAX status report, arXiv:2003.10894.
[106] R. G. Povey, J. G. Hartnett, and M. E. Tobar, Microwave cavity light shining through a wall optimization and experiment, Phys. Rev. D **82**, 052003 (2010).
[107] J. Redondo and A. Ringwald, Light shining through walls, Contemp. Phys. **52**, 211 (2011).
[108] S. Gninenko, Search for MeV dark photons in a light-shining-through-walls experiment at CERN, Phys. Rev. D **89**, 075008 (2014).
[109] J. T. Mendonça, J. D. Rodrigues and H. Terças, Axion production in unstable magnetized plasmas, Phys. Rev. D **101**, 051701 (2020).

[110] A. D. Spector, *Light-Shining-Through-Walls Experiments* (Springer International Publishing, Cham, 2023), pp. 255–279.
[111] I. V. Semchenko, S. A. Khakhomov, S. A. Tretyakov, and A. H. Sihvola, Electromagnetic waves in artificial chiral structures with dielectric and magnetic properties, Electromagnetics **21**, 401 (2001).
[112] A. Christofi and N. Stefanou, Metal-coated magnetic nanoparticles in an optically active medium: A nonreciprocal metamaterial, Phys. Rev. B **97**, 125129 (2018).
[113] S. F. Koufidis, T. T. Koutserimpas, F. Monticone, and M. W. McCall, Electromagnetic wave propagation in time-periodic chiral media, Opt. Mater. Express **14**, 3006 (2024).
[114] F. R. Prudencio, S. A. Matos, and C. R. Paiva, A geometrical approach to duality transformations for tellegen media, IEEE Trans. Microwave Theory Tech. **62**, 1417 (2014).
[115] L. Shaposhnikov, M. Mazanov, D. A. Bobylev, F. Wilczek, and M. A. Gorlach, Emergent axion response in multilayered metamaterials, Phys. Rev. B **108**, 115101 (2023).
[116] S. Safaei Jazi, I. Faniayeu, R. Cichelero, D. C. Tzarouchis, M. M. Asgari, A. Dmitriev, S. Fan, and V. Asadchy, Optical Tellegen metamaterial with spontaneous magnetization, Nat. Commun. **15**, 1293 (2024).
[117] Q. Yang, X. Wen, Z. Li, O. You, and S. Zhang, Gigantic Tellegen responses in metamaterials, Nat. Commun. **16**, 151 (2025).
[118] T. Z. Seidov and M. A. Gorlach, Unbounded Tellegen response in media with multiple resonances, Phys. Rev. A **111**, 033521 (2025).
[119] S. Safaei Jazi, I. Faniayeu, R. Cichelero, N. Kuznetsov, S. van Dijken, S. Fan, A. Dmitriev, and V. Asadchy, Realization of the Tellegen effect in resonant optical metasurfaces, eLight **6**, 8 (2026).